SAND2017-12413J

Squeezing clathrate cages to host trivalent rare-earth guests

Jian Wang[a,b], Yuping He[c], Natalia E. Mordvinova[d], Oleg Lebedev[d], Kirill Kovnir[a,b,*]

[a] Department of Chemistry, Iowa State University, Ames, IA 50010, United States

[b] Ames Laboratory, Ames, Iowa 50011, United States

[c] Sandia National Laboratories, 7011 East Avenue, Livermore, CA 94551, United States

[d] Laboratoire CRISMAT, ENSICAEN, CNRS UMR 6508, F-14050 Caen, France

Abstract

Strike difference of the trivalent rare-earth cations from their alkali and alkaline-earth peers is in the presence of localized 4*f*-electrons and strong spin-orbit coupling. Placing trivalent rare-earth cations inside the fullerene molecules or in between the blocks of itinerant magnetic intermetallics gave rise to plethora of fascinating properties and materials. A long-time missing but hardly desired piece is the semiconducting or metallic compound where rare-earth cations are situated inside the oversized polyhedral cages of three-dimensional framework. In this work we present a synthesis of such compounds, rare-earth containing clathrates $Ba_{8-x}R_xCu_{16}P_{30}$. The unambiguous proofs of their composition and crystal structure were achieved by a combination of synchrotron powder diffraction, time-of-flight neutron powder diffraction, scanning-transmission electron microscopy, and electron energy-loss spectroscopy. Our quantum-mechanical calculations and experimental characterizations show that the incorporation of the rare-earth cations significantly enhances the hole mobility and concentration which results in the drastic increase in the thermoelectric performance.

Rattler-type moieties with rare-earth *f*-metals encapsulated inside covalent cages are fascinating objects of high fundamental and applied importance. Chemistry of molecular examples, endohedral fullerenes trapping rare-earth metals, is well-developed (Fig. 1a) [1,2]. Fusing the molecular cages together at extreme pressures of hundreds GPa was predicted to induce room-temperature superconductivity when carbon is replaced with hydrogen (Fig. 1b) [3]. At ambient pressure superconductivity has been achieved in compounds where a cage with smaller number of vertices encapsulating trivalent rare-earth cation was a part of complex crystal structure [4]. In addition to superconductivity, the interactions between rare-earth guests and framework cages give rise to diverse physical properties such as magnetic and quadrupole ordering to heavy-fermion and non-Fermi liquids, itinerant ferromagnetism, and half-metallicity (Figs. 1c and 1d) [5-9].

In these examples rare-earth containing cages are isolated from each other. Fusing of all cages together to achieve voids-free tiling of space is possible in clathrates, which are formed by heavy carbon analogues, Si, Ge, and Sn (Fig. 1e). Clathrate cages, such as 20-vertex pentagonal dodecahedron or 24-vrtex tetrakaidecahedron, are larger than aforementioned rare-earth containing cages, requiring large mono or divalent cations as guest rattlers inside clathrate frameworks. Clathrates with Ba^{2+} and Eu^{2+} guests were shown to exhibit a wide-range of properties, such as superconductivity, ultra-low thermal conductivity, and giant magnetocaloric effect [10-13].

Incorporation of the trivalent rare-earth guests into clathrate is a long-desired but hard to achieve goal [14-15]. Strongly-correlated behavior with exotic properties

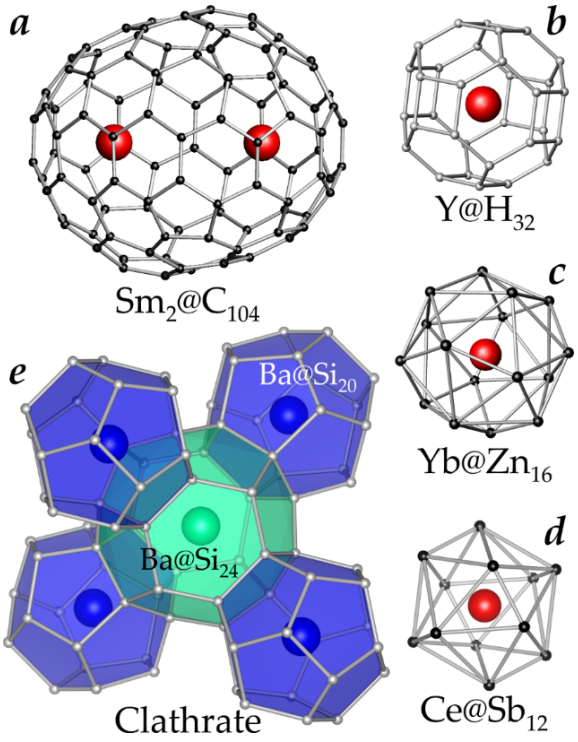

Figure 1. Rattler-type cages: (a) A molecule of fullerene C_{104} encapsulating two Sm atoms [2]; isolated fragments of the crystal structure of (b) predicted YH_{10} hydride [3], (c) $YbIr_2Zn_{20}$ intermetallic [6], and (d) $CeCo_4Sb_{12}$ skutterudite [8]; (e) a fragment of the extended structure of clathrate Ba_8Si_{46} [10] with 20-vertex pentagonal dodecahedra shown in blue and 24-vertex tetrakaidecahedron shown in green.

was predicted to arise from the interactions between localized 4*f* electrons of guest cations and conduction electrons of clathrate. Multiple reported unsuccessful attempts pursuing the synthesis of rare-earth containing clathrates [16,17] are just the top of the iceberg of much higher number of experiments documented only in lab journals all over the world. Similarity of the X-ray scattering factors of rare-earth and neighboring Ba elements, segregation of the rare-earth atoms to secondary phase and/or to the phase boundaries, change of the unit cell volume due to adjustment of the framework composition, unavailability of the high-quality single crystals are the main reasons preventing unambiguous identification of the rare-earth substitution in the clathrate structure. Only one reliable example reported up to today is $R_1Ba_8Au_6Si_{40}$ (R = La, Ce), in which the comprehensive float-zone technique was applied to incorporate rare-earth elements into the clathrate cage [18]. This report stimulated our search for the rare-earth clathrate with inexpensive framework elements, commonly accessible synthetic methodology, and unambiguous proofs of the incorporation of rare-earth into the clathrate structure.

In the clathrates, the matching between the guest atom size and framework sizes is crucial for the stability [19]. Cations serving as guest atoms in clathrates are Cs^+ (1.74 Å), Rb^+ (1.61 Å), K^+ (1.51 Å), Ba^{2+} (1.46 Å), Sr^{2+} (1.26 Å), Eu^{2+} (1.25 Å), Na^+ (1.18 Å) [20]. It is challenging to incorporate the rare-earth elements into the clathrate cages due to the smaller radius of rare-earth elements; even for the largest rare-earth trivalent cation, La^{3+}, an ionic radius (1.16 Å) is smaller than that for Na^+. The latter cation can be only stabilized in the structure of the smallest, Si-based clathrate frameworks. A clathrate with trivalent rare-earth guests would require frameworks with effective radii of the framework atoms equal to or smaller than those for Si. This can be realized in Cu-P clathrate frameworks which are versatile in respect to their chemical bonding and cages sizes and topology [21-23]. The smallest among all clathrate cages have been realized in $Ba_8Cu_{16}P_{30}$, where pentagonal dodecahedra with volumes of 97.4 $Å^3$ and 101.5 $Å^3$ are present. Those cages have reduced volume compared to the cages in the smallest Si-based clathrates: Na_8Si_{46} (103.9 $Å^3$), $K_8B_7Si_{39}$ (104.2 $Å^3$), and $Ba_8Au_5Si_{41}$ (108.0 $Å^3$) [24-26]. Moreover, the 2% volume reduction of dodecahedral cages down to 95.3 Å was demonstrated by incorporation of Eu^{2+} in $Ba_{8-x}Eu_xCu_{16}P_{30}$ [27]. Our computations predict that fully relaxed hypothetical compound $Ba_6La_2Cu_{16}P_{30}$ will exhibit reduction of the volume of pentagonal dodecahedra by 5% as compared to $Ba_8Cu_{16}P_{30}$. Unlike isovalent Ba^{2+}/Eu^{2+} substitution, the aliovalent Ba^{2+}/R^{3+} substitution induces a charge disbalance. Advantageously, the valence band of $Ba_8Cu_{16}P_{30}$ is unfilled and has a capacity to

accept two electrons per formula unit [21,22]. Thus, $Ba_8Cu_{16}P_{30}$ is a suitable platform for the incorporation of trivalent rare-earth metals.

Herein we present a simple solid-state synthesis method to incorporate La and Ce rare-earth cations into the guest sublattice of $Ba_8Cu_{16}P_{30}$. The incorporation of rare-earth elements was directly proved by a combination of electron microprobe analysis (EPMA), synchrotron powder X-ray and neutron diffraction techniques, high-resolution scanning-transmission electron microscopy (STEM), and atomic resolution electron energy loss spectroscopy (EELS). The Ba^{2+}/R^{3+} substitution greatly affects the charge carrier concentration and mobility resulting in an order of magnitude enhancement of thermoelectric (TE) efficiency which is confirmed by the thorough *ab initio* calculations. The developed synthetic method is commonly available to materials scientists interested in the *f*-elements clathrates.

The polycrystalline clathrate samples were synthesized using conventional solid-state technique, by annealing corresponding elements in evacuated silica ampoules at 1123 K for three times. The uniform distribution of the elements and compositions of produced clathrate samples were determined by electron microprobe analysis (EMPA). Powder diffraction patterns exhibit a systematic peak shift to the higher diffraction angles with the rare-earth content increase indicating a reduction of the unit cell volume. No substantial alteration of the Cu/P ratio in the framework was observed by EMPA (Table S1). X-ray diffraction is not suitable to distinguish between La and Ba atoms due to similar X-ray scattering factors for these elements. Neutron coherent lengths for La and Ba are quite different, 8.2 fm and 5.1 fm respectively. Rietveld refinement of the time-of-flight neutron diffraction pattern for sample with EPMA-determined cation ratio $Ba_{7.1(1)}La_{0.9(1)}$ unambiguously reveals the excessive nuclear density at the positions inside the pentagonal dodecahedra when those positions are refined as Ba only. Refinement of those positions as mixed occupied by La and Ba atoms resulted in significant improvement of the refinement and final composition of $Ba_{7.1}La_{0.8(2)}Cu_{16}P_{30}$ (Figure 2B).

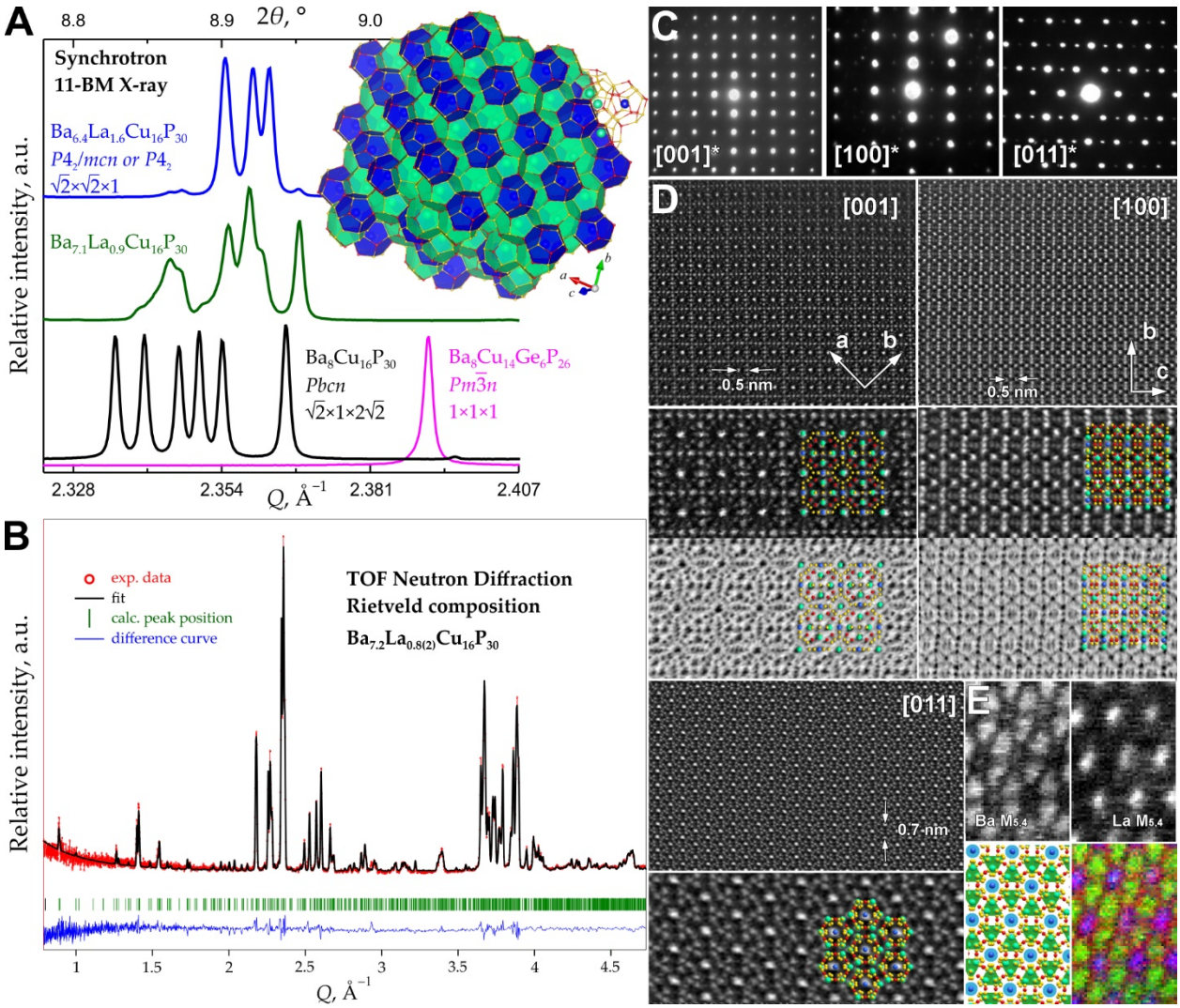

Figure 2. (A) Fragments of synchrotron powder diffraction patterns for $Ba_{8-x}La_xCu_{16}P_{30}$ (x = 0, 0.9, and 1.6) and $Ba_8Cu_{14}Ge_6P_{26}$. Inset shows the clathrate I crystal structure with smaller pentagonal dodecahedra shown in blue and larger tetrakaidecahedra shown in green. (B) Rietveld refinement of the time-of-flight neutron powder diffraction pattern for $Ba_{7.1}La_{0.9}Cu_{16}P_{30}$. (C and D) electron diffraction patterns and STEM high resolution HAADF and ABF images for the three main zones of tetragonal $Ba_{6.4}La_{1.6}Cu_{16}P_{30}$ with overlaid structural fragments. (E) Atomic resolution EELS for [011] zone of $Ba_{6.4}La_{1.6}Cu_{16}P_{30}$.

Synchrotron powder X-ray diffraction investigation confirms the peak shift and shows that a clear structural transition occurs for a sample with high La concentration (Figures 2A and S1). The main diffraction peak in the diffraction pattern of an arystotype of clathrate-I, such as $Ba_8Cu_{14}Ge_6P_{26}$ (cubic space group $Pm\bar{3}n$), is split into six distinct peaks in the structure of $Ba_8Cu_{16}P_{30}$ (orthorhombic space group *Pbcn*) due to Cu and P segregation over 23 different framework

positions [27]. Similar splitting persists in the diffraction pattern of $Ba_{7.1}La_{0.9}Cu_{16}P_{30}$. Further increase of La content resulted in the structural transition as evidenced by the presence of only three main peaks at $Q = 2.35$ Å^{-1} in the diffraction pattern of $Ba_{6.4}La_{1.6}Cu_{16}P_{30}$. In the latter case, all the intense diffraction peaks can be indexed in the primitive tetragonal cell, $a = 14.0655(7)$ Å, $c = 10.0037(6)$ Å (Figure S2). The systematic absences indicate the presence of 4_2 screw axis, the absence of the diagonal *c*-glide plane, and allow for (001) *n*- and (100) *c*-glide planes. Such absences rule out the $P4_2/mmc$ space group, but allow for multiple groups ranging from $P4_2$ to $P4_2/ncm$. A significant difference of the tetragonal $\sqrt{2}\times\sqrt{2}\times1$ $P4_2$ or $P4_2/ncm$ clathrate superstructures from the orthorhombic $2\sqrt{2}\times1\times\sqrt{2}$ *Pbcn* superstructure is the number of unique types of small dodecahedral cages. There is only one such cage in the tetragonal structure of $Ba_{6.4}La_{1.6}Cu_{16}P_{30}$ and two dodecahedral cages in the orthorhombic structure of $Ba_8Cu_{16}P_{30}$ (Figure S3) [19]. $\sqrt{2}\times\sqrt{2}\times1$ tetragonal superstructure is the first report of the clathrate superstructure caused not by vacancies ordering in the guest sublattice but due to a mismatch between the sizes of the two types of guest atoms, La and Ba.

The tetragonal superstructure was confirmed by the electron microscopy investigation (Figures 2C and S4-S5). Electron diffraction patterns can be indexed in the primitive tetragonal cell, $a = \sim14.06$ Å, $c = \sim10.00$ Å. High-resolution images are in good agreement with the structural models. Finally, the presence of La in the crystal structure of $Ba_{6.4}La_{1.6}Cu_{16}P_{30}$ was confirmed by atomic resolution EELS (Figures 2D and S6). Structural model shown in Figure 1D was created by placing La atoms in the smaller pentagonal dodecahedra and larger Ba atoms inside tetrakaidecahedra. Our detailed structural analyses unambiguously show that La was indeed incorporated to the small cages of Cu-P clathrate I framework.

Tetrahedrally-coordinated Cu and P atoms require 4 electrons per atom to realize an electron octet by forming 4 covalent bonds. With one valence electron from Cu, five from P, and full donation of two valence electrons from Ba to framework, the $Ba_8Cu_{16}P_{30}$ is an electron-deficient compound, with 182 total valence electrons [1×16 (Cu)] + [5×30 (P)] + [2×8 (Ba)] instead of the required 184 = 46×4. The location of the Fermi level in the valence bands is confirmed by the *ab initio* calculations (Figure 3A) and properties measurements. In accordance with the predictions, $Ba_8Cu_{16}P_{30}$ exhibits temperature-independent Pauli paramagnetism. Similar behavior was observed for $Ba_{7.1}La_{0.9}Cu_{16}P_{30}$ (Figure S7). In contrast, $Ba_{7.3}Ce_{0.7}Cu_{16}P_{30}$ exhibit a sharp upturn of

magnetic susceptibility, χ, at low temperatures, which is typical for a Curie-Weiss behavior (Figure S7). Nevertheless, no satisfactory Curie-Weiss fit was achieved for the whole temperature range with or without including a temperature-independent contribution. Curie-Weiss fit performed for the data in narrow temperature ranges resulted in an effective moment of 2.3-2.5 μ_B/Ce which is slightly smaller than the theoretical value of 2.54 μ_B for Ce^{3+}. The χT temperature dependence reveal complex magnetic behavior with two cusps centered at 53 K and 7 K (Figure S7). At 53 K a clear change in the slope of the temperature dependence of resistivity was observed. Such non-classical magnetic behavior may originate from the interactions of Ce 4*f*-electrons with the valence band electrons and warrants further investigation which will be performed on samples with variable Ce content.

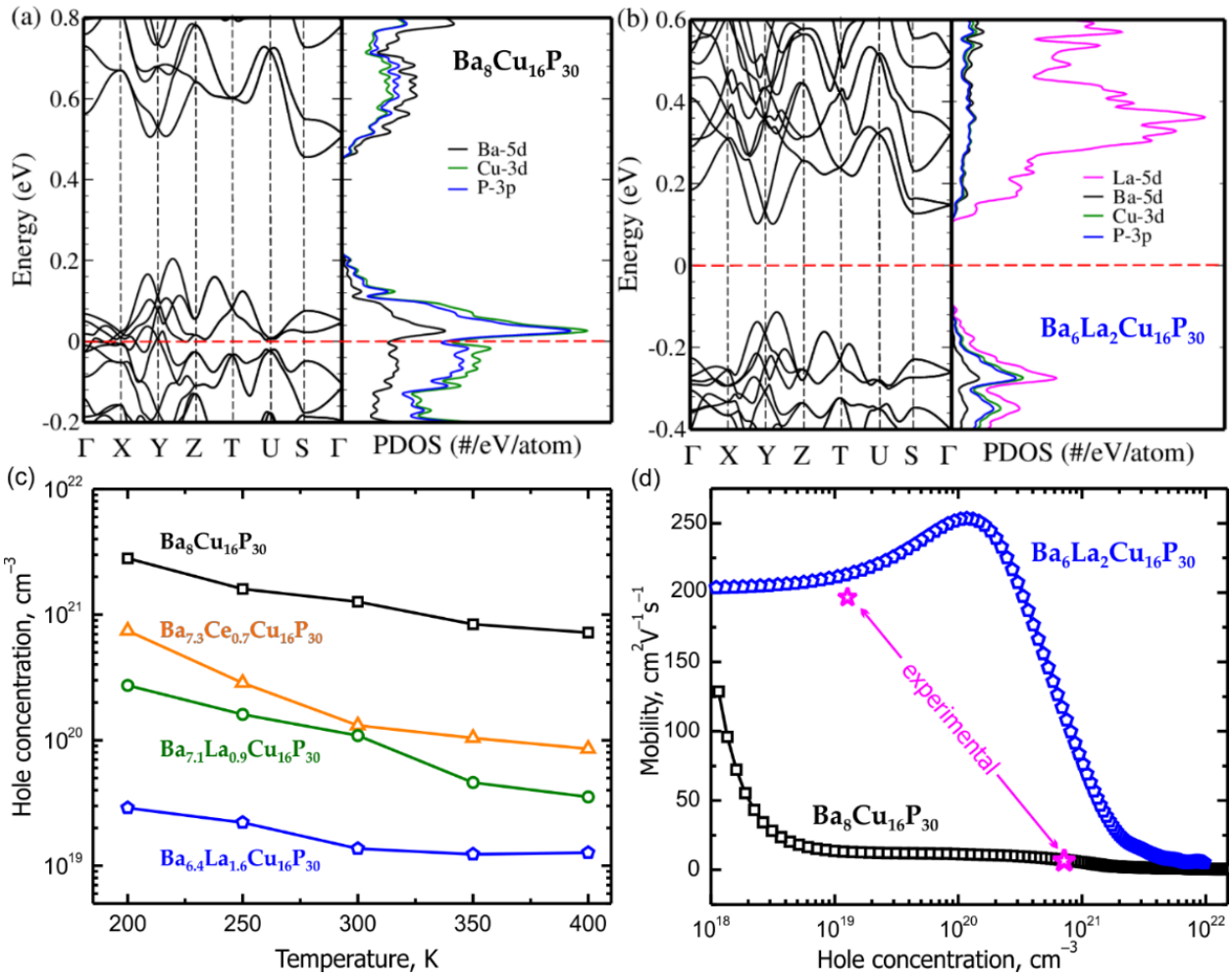

Figure 3. (A and B) Band structures and atomic partial density of states for $Ba_8Cu_{16}P_{30}$ and hypothetical $Ba_6La_2Cu_{16}P_{30}$. The red dash line represents the Fermi level. The partial density of states with contributions from Ba 5*d*-orbitals (black), Cu 3*d*-orbitals (green), P 3*p*-orbitals (blue)

and La 5*d*-orbitals (pink). (C) Experimental temperature dependence of the hole concentration for $Ba_{8-x}La_xCu_{16}P_{30}$ (x = 0, 0.9, and 1.6) and $Ba_{7.3}Ce_{0.7}Cu_{16}P_{30}$. (D) Calculated hole mobilities for $Ba_8Cu_{16}P_{30}$ and hypothetical $Ba_6La_2Cu_{16}P_{30}$; experimental mobilities for $Ba_8Cu_{16}P_{30}$ and $Ba_{6.4}La_{1.6}Cu_{16}P_{30}$ are shown as magenta stars.

The replacement of Ba^{2+} with La^{3+} (or Ce^{3+}) increases the total number of valence electrons ultimately leading to the electron-balanced composition $Ba_6La_2Cu_{16}P_{30}$ with exactly 184 electrons per formula unit. This composition is predicted to be an intrinsic semiconductor (Figure 3B). We found that the complete electron-balanced composition was not achieved in our synthesis, but the expected reduction of the hole concentration upon the increase of the rare-earth content was observed as revealed by the Hall effect measurements (Figure 3C). Such drastic change in the hole concentration is not accompanied with the substantial modification of the carrier effective mass (Table S2), but significantly affects the hole mobility, which increases by a factor of 30, from 6.6 $cm^2V^{-1}s^{-1}$ to 197 $cm^2V^{-1}s^{-1}$ at 400 K for $Ba_8Cu_{16}P_{30}$ and $Ba_{6.4}La_{1.6}Cu_{16}P_{30}$, respectively (Figures 2D and S12). The hole mobility for $Ba_{6.4}La_{1.6}Cu_{16}P_{30}$ is 4-5 times higher than the mobilities for the Si-based clathrates [28].

Modification of both charge carrier concentration and mobility upon the incorporation of the rare-earth elements into clathrate called for the thermoelectric properties characterization (Figures 4 and S8-S11). Polycrystalline samples were pressed into high-density pellets using spark plasma sintering. The increases in the thermopower and electrical resistivity with rare-earth content are consistent with the computational predictions. The *ab initio* calculated Seebeck coefficients of $Ba_8Cu_{16}P_{30}$ and $Ba_{6.4}La_{1.6}Cu_{16}P_{30}$ samples (Figure S13) are qualitatively consistent with the measured values. The smaller experimental values for La containing phase could be due incomplete small variation in experimental composition (exp. $Ba_{6.4}La_{1.6}Cu_{16}P_{30}$; calc. $Ba_6La_2Cu_{16}P_{30}$) or due to structural defects and grain boundaries in the sintered samples. All the samples exhibit metallic behavior with resistivity increasing with temperature in accordance to the determined compositions, electron count, and calculations, indicating that less than two rare-earth metals per formula unit were incorporated.

The thermal conductivities of the rare-earth containing samples remain below 1.2 $Wm^{-1}K^{-1}$, while pristine $Ba_8Cu_{16}P_{30}$ exhibits higher thermal conductivity of 1.4 $Wm^{-1}K^{-1}$. This is due to diminishing contribution of the charge carrier component (Figure 4C). For the lattice contribution

to the total thermal conductivity, the trend is opposite, the most complex structure, pristine orthorhombic $Ba_8Cu_{16}P_{30}$ exhibits the lowest lattice thermal conductivity, while less complex tetragonal $La_{1.6}Ba_{6.4}Cu_{16}P_{30}$ possesses higher lattice thermal conductivity. Nonetheless, the totoal and lattice thermal conductivities for all the studied clathrates are very low and comparable with those for the state-of-the-art thermoelectric materials [15,19,29-33]. Rare-earth incorporation leads to the enhancement of Seebeck and suppression of the total thermal conductivity resulting in a significant improvement of thermoelectric figure-of-merit, $zT = S^2T/\rho\kappa$, where S is the thermopower, T is the absolute temperature, ρ is the electrical resistivity, and κ is the total thermal conductivity. $La_{1.6}Ba_{6.4}Cu_{16}P_{30}$ shows the highest efficiency, 0.11 at 300 K to 0.63 at 900 K, compared to poor efficiency of $Ba_8Cu_{16}P_{30}$, 0.01 at 300 K to 0.09 at 900 K. 700% enhancement of thermoelectric efficiency due to rare-earth doping is a substantial achievement compared to incremental 20-40% increases which are typical to the thermoelectric field [19,29]. Moreover, the flexible Cu-P clathrate framework provides room for further improvement of the thermoelectric efficiency.

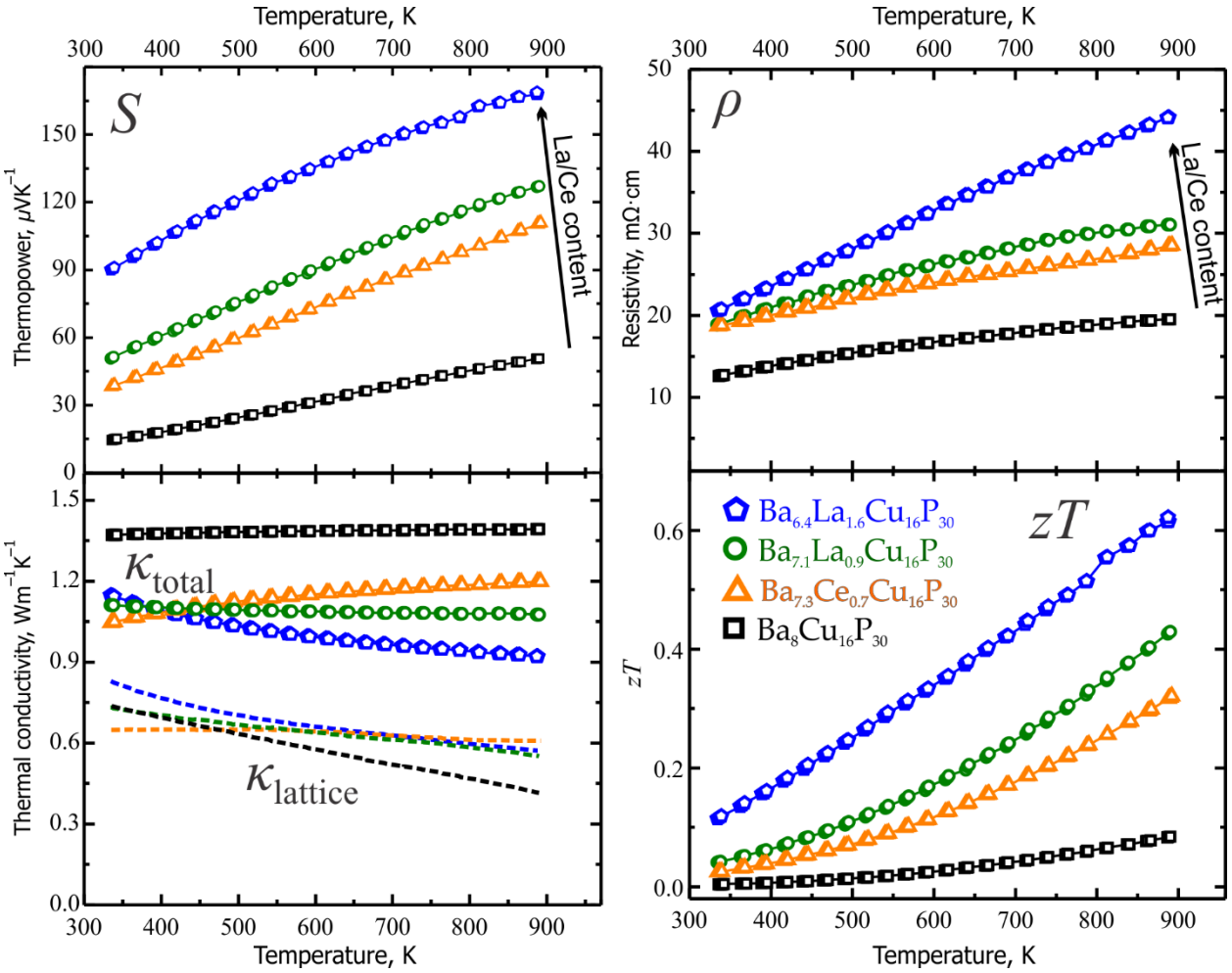

Figure 4. Transport properties of $Ba_{8-x}La_xCu_{16}P_{30}$ (x = 0, 0.9, and 1.6) and $Ba_{7.3}Ce_{0.7}Cu_{16}P_{30}$. Top left: thermopower; top right: electrical resistivity; bottom left: thermal conductivity with lattice contribution shown as dashed lines; bottom right: thermoelectric figure of merit, zT.

Through simplest solid-state reaction, the rare-earth elements, La and Ce, were successfully incorporated into the pentagonal dodecahedral cages of clathrate $Ba_8Cu_{16}P_{30}$. Synchrotron X-ray diffraction and neutron powder diffractions together with atomic resolution EELS and STEM studies unambiguously demonstrated the residence of rare-earth elements in the clathrate cages. The remarkably enhanced TE efficiency is mainly due to the reduction of hole concentration, resulted by the better electron-balancing from the substitution of La^{3+} (or Ce^{3+}) with respect to $Ba_8Cu_{16}P_{30}$, which is confirmed by both experimental measurements and theoretical calculations. An example of the 700% enhancement of the thermoelectric performance demonstrated high potential of the rare-earth incorporation for the modification of the electronic structure and properties of clathrates. We believe that the tunable clathrate framework combined with readily

accessible synthetic method will inspire chemistry, physics, and materials science research on the rare-earth containing clathrates.

Methods

Synthesis. All preparation and handling of samples were performed in an argon-filled glovebox with the O_2 level below 1 ppm. All starting materials are commercial grade and were used as received: sublimed Ba crystals (Sigma-Aldrich, 99.9%), La powder (Alfa Aesar, 99.9%), Ce chunks (Ames Laboratory, 99.996 %), Cu powder (Sigma-Aldrich, 99.9%), and red P powder (Alfa Aesar, 99 %). The polycrystalline samples of La/Ce-substituted $Ba_8Cu_{16}P_{30}$ were synthesized by solid-state reactions of elements. The elements in *R*/Ba/Cu/P = 8–*x*/*x*/16/30 (*R* = La, Ce; *x* = 0, 1, 2, 3) ratios were loaded into carbonized silica ampoules, evacuated, and flame-sealed. The ampoules were heated from room temperature to 1123 K over 17 h, and annealed at this temperature for 144 hours. After the furnace was turned off, the samples were grinded and reloaded to new ampoules in the glovebox, resealed, and reheated using the same temperature profile. The grinding/reannealing procedure was repeated for a third time. After three annealing, the uniform powder was formed, which was further characterized. X-ray powder diffraction indicates the significant amounts of the admixtures for *x* = 3 (La) an *x* = 2 and 3 (Ce) nominal compositions.

The samples were characterized by EPMA microanalysis, conventional and synchrotrotn X-ray powder diffraction, neutron powder diffraction, and scanning transmission elecron microscopy and electron energy-loss spectroscopy. Electronic structures were calculated using *ab initio* density functional theory (DFT) implemented in the Vienna simulation package (VASP). The thermoelectric transport properties were computed using the Landauer formalism in the linear response regime. Magnetic properties were characterized with Quantum Design MPMS-XL SQUID magnetometer. Powdered samples were compacted using Spark Plasma Sintering and transport properties were studied. High resolution synchrotron XRD were collected at beamline 11-BM at the Advanced Photon Source (APS) at Argonne National Lab (ANL). Neutron powder diffraction time-of-flight data was collected at the POWGEN beamline at the Spallation Neutron Source (SNS) at Oak Ridge National Laboratory (ORNL). Further synthetic, characterization, and calculation details can be found in the supporting information.

Acknowledgement

The authors wish to thank Prof. S. M. Kauzlarich (UC Davis) for use of SPS, LFA, and LSR-3 equipment; S. Lapidus at the APS ANL for collecting synchrotron XRD patterns; and Ashfia Huq at the SNS ORNL for help with the neutron diffraction measurements. This research was supported by the U.S. Department of Energy, Office of Basic Energy Sciences, Division of Materials Science and Engineering under Award DE-SC0008931. Use of the Advanced Photon Source at Argonne National Laboratory was supported by the U.S. Department of Energy, Office of Science, Office of Basic Energy Sciences, under Contract No. DE-AC02-06CH11357. Research conducted at ORNL's Spallation Neutron Source was sponsored by the Scientific User Facilities Division, Office of Basic Energy Sciences, U.S. Department of Energy. The theoretical calculations were performed on Sandia cluster. Sandia National Laboratories is a multi-mission laboratory managed and operated by National Technology and Engineering Solutions of Sandia, LLC, a wholly owned subsidiary of Honeywell International, Inc., for the U.S. Department of Energy's National Nuclear Security Administration under contract DE-NA0003525.

References

1. Stevenson, S.; Rice, G.; Glass, T.; Harich, K.; Cromer, F.; Jordan, M. R.; Craft, J.; Hadju, E.; Bible, R.; Olmstead, M. M.; Maitra, K.; Fisher, A. J.; Balch, A. L.; Dorn, H. C. Small-bandgap endohedral metallofullerenes in high yield and purity. *Nature* **1999,** *401,* 55-57.
2. Mercado, B. Q.; Jiang, A.; Yang, H.; Wang, Z.; Jin, H.; Liu, Z.; Olmstead, M. M.; Balch, A. L. Isolation and Structural Characterization of the Molecular Nanocapsule $Sm_2@D_{3d}(822)$-C_{104}. *Angew. Chem. Int. Ed.* **2009,** *48,* 9114-9116.
3. Peng, F.; Sun, Y.; Pickard, C. J.; Needs, R. J.; Wu, Q.; Ma, Y. Hydrogen Clathrate Structures in Rare Earth Hydrides at High Pressures: Possible Route to Room-Temperature Superconductivity. *Phys. Rev. Lett.* **2017,** *119,* 107001.
4. Gumeniuk, R.; Schnelle, W.; Rosner, H.; Nicklas, M.; Leithe-Jasper, A.; Grin, Yu. Superconductivity in the Platinum Germanides MPt_4Ge_{12} (M = Rare-Earth or Alkaline-Earth Metal) with Filled Skutterudite Structure *Phys. Rev. Lett.* **2008,** *100,* 017002.
5. Keppens, V.; Mandrus, D.; Sales, B. C.; Chakoumakos, B. C.; Dai, P.; Coldea, R.; Maple, M. B.; Gajewski, D. A.; Freeman, E. J.; Bennington, S. Localized vibrational modes in metallic solids. *Nature* **1998,** *395,* 876-878.
6. Torikachvili, M. S.; Jia, S.; Mun, E. D.; Hannahs, S. T.; Black, R. C.; Neils, W. K.; Martien, D.; Bud'ko, S. L.; Canfield, P. C. Six closely related YbT_2Zn_{20} (T = Fe, Co, Ru, Rh, Os, Ir)

heavy fermion compounds with large local moment degeneracy. *Proc. Natl. Acad. Sci.* **2007,** *104,* 9960-9963.

7. Leithe-Jasper, A.; Schnelle, W.; Rosner, H.; Senthilkumaran, N.; Rabis, A.; Baenitz, M.; Gippius, A.; Morozova, E.; Mydosh, J. A.; Grin, Yu. Ferromagnetic Ordering in Alkali-Metal Iron Antimonides: $NaFe_4Sb_{12}$ and KFe_4Sb_{12}. *Phys. Rev. Lett.* **2003,** *91,* 037208.
8. Sales, B.C.; Mandrus, D.; Williams, R.K. Filled skutterudite antimonides: A new class of thermoelectric materials. *Science,* **1996,** *272*, 1325-1328.
9. Goldman A. I.; Kong, T.; Kreyssig, A.; Jesche, A.; Ramazanoglu, M.; Dennis, K. W.; Bud'ko, S. L.; Canfield, P.C. A family of binary magnetic icosahedral quasicrystals based on rare-earths and cadmium. *Nature Mater.* **2013,** *12,* 714-718.
10. Tanigaki, K.; Shimizu, T.; Itoh, K. M.; Teraoka, J.; Moritomo, Y.; Yamanaka, S. Mechanism of superconductivity in the polyhedral-network compound Ba_8Si_{46}. *Nature Mater.* **2003,** *2,* 653-655.
11. Guloy, A.M.; Ramlau, R.; Tang, Z.; Schnelle, W.; Baitinger, M.; Grin, Yu. A guest-free germanium clathrate. *Nature* **2006,** *443*, 320-323.
12. Phan, M. H.; Woods, G. T.; Chaturvedi, A.; Stefanoski, S.; Nolas, G. S. Long-range ferromagnetism and giant magnetocaloric effect in type VIII $Eu_8Ga_{16}Ge_{30}$ clathrates. *Appl. Phys. Lett.* **2008,** *93,* 252505.
13. Lory, P.-F.; Pailhès, S.; Giordano, V. M.; Euchner, H.; Nguyen, H. D.; Ramlau, R.; Borrmann, H.; Schmidt, M.; Baitinger, M.; Ikeda, M.; Tomeš, P.; Mihalkovič, M.; Allio, C.; Johnson, M. R.; Schober, H.; Sidis, Y.; Bourdarot, F.; Regnault, L. R.; Ollivier, J.; Paschen, S.; Grin, Yu.; de Boissieu, M. Direct measurement of individual phonon lifetimes in the clathrate compound $Ba_{7.81}Ge_{40.67}Au_{5.33}$. *Nature Commun.* **2017,** *8,* 491.
14. Si, Q.; Steglich, F. Heavy Fermions and Quantum Phase Transitions. *Science,* **2010,** *329,* 1161-1166.
15. The physics and chemistry of inorganic clathrates. Ed. Nolas, G. S. Springer, **2014**.
16. Pacheco, V.; Carrillo-Cabrera, W.; Tran, V. H.; Paschen, S.; Grin, Yu. Comment on "Silicon Clathrate with an f-Electron System" *Phys. Rev. Lett.* **2000,** *87,* 099601.
17. Paschen, S.; Gspan, C.; Grogger, W.; Dienstleder, M.; Laumann, S.; Pongratz, P.; Sassika, H.; Wernisch, J.; Prokofiev, A. Investigation of Yb substitution in the clathrate phase $Eu_8Ga_{16}Ge_{30}$. *J. Crystal Growth* **2008,** *310,* 1853-1858.
18. Prokofiev, A.; Sidorenko, A.; Hradil, K.; Ikeda, M.; Svagera, R.; Waas, M.; Winkler, H.; Neumaier, K.; Paschen, S. Thermopower enhancement by encapsulating cerium in clathrate cages. *Nature Mater.* **2013,** *12,* 1096-1101.
19. Dolyniuk, J.; Owens-Baird, B.; Wang, J.; Zaikina, J.V.; Kovnir, K. Thermoelectric clathrates. *Mat. Sci. Eng. R* **2016,** *108,* 1-46.
20. Shannon, R. D. Revised effective ionic radii and systematic studies of interatomic distances in halides and chalcogenides. *Acta Crystallogr. A* **1976,** *32,* 751-767.

21. Dolyniuk, J.; Whitfield, P.S.; Lee, K.; Lebedev, O.I.; Kovnir, K. Controlling Superstructural Ordering in the Clathrate-I $Ba_8Cu_{16}P_{30}$ (M= Cu, Zn) through the Formation of Metal-Metal Bonds. *Chem. Sci.* **2017**, *8*, 3650-3659.

22. Wang, J.; Lebedev, O.I.; Lee, K.; Dolyniuk, J.; Klavins, P.; Bux, S.; Kovnir, K. A high-efficiency thermoelectric $Ba_8Cu_{14}Ge_6P_{26}$: Bridging the gap between tetrel-based and tetrel-free clathrates. *Chem. Sci.* **2017,** *DOI: 10.1039/C7SC03482B.*

23. Dolyniuk, J.; Zaikina, J.V.; Kaseman, D.C.; Sen, S.; Kovnir, K. Breaking the Tetra-Coordinated Framework Rule: New Clathrate $Ba_8M_{24}P_{28+\delta}$ (M = Cu/Zn). *Angew. Chem. Int. Ed.* **2017,** *56,* 2418-2422.

24. Beekman, M.; Nenghabi, E. N.; Biswas, K.; Myles, C. W.; Baitinger, M.; Grin, Yu.; Nolas, G. S. Framework contraction in Na-stuffed Si(*cF*136). *Inorg. Chem.* **2010,** *49,* 5338-5340.

25. Jung, W.; J. Lörincz, J.; Ramlau, R.; Borrmann, H.; Prots, Yu.; Haarmann, F.; Schnelle, W.; Burkhardt, U.; Baitinger, M.; Grin, Yu. $K_7B_7Si_{39}$, a Borosilicide with the Clathrate I Structure *Angew. Chem. Int. Ed.* **2007,** *46,* 6725-6728.

26. Zeiringer, I.; Chen, M.; Grytsiv, A.; Bauer, E.; Podloucky, R.; Effenberger, H.; Rogl, P. The ternary system Au-Ba-Si: Clathrate solution, electronic structure, physical properties, phase equilibria and crystal structures. *Acta Mater.* **2012,** *60,* 2324-2336.

27. Kovnir, K.; Stockert, U.; Budnyk, S.; Prots, Yu.; Baitinger, M.; Paschen, S.; Shevelkov, A. V.; Grin, Yu. Introducing a Magnetic Guest to a Tetrel-Free Clathrate: Synthesis, Structure, and Properties of $Eu_xBa_{8-x}Cu_{16}P_{30}$ ($0 \leq x \leq 1.5$). *Inorg. Chem.* **2011,** *50,* 10387-10396.

28. He, Y.; Sui, F.; Kauzlarich, S. M.; Galli, G. Si-based Earth abundant clathrates for solar energy conversion. *Energy Environ. Sci.* **2014,** *7,* 2598-2602.

29. Owens-Baird, B.; Heinrich, S.; Kovnir, K. Thermoelectric Materials. *Encyclopedia of Inorganic and Bioinorganic Chemistry.* **2017,** 1-35.

30. Brown, S. R.; Kauzlarich, S. M.; Gascoin, F.; Snyder, G. J. $Yb_{14}MnSb_{11}$: New High Efficiency Thermoelectric Material for Power Generation. *Chem. Mater.* **2006,** *18,* 1873-1877.

31. Poudel, B.; Hao, Q.; Ma, Y.; Lan, Y.; Minnich, A.; Yu, B.; Yan, X.; Wang, D.; Muto, A.; Vashaee, D.; Chen, X.; Liu, J.; Dresselhaus, M. S.; Chen, G.; Ren, Z. F. High-thermoelectric performance of nanostructured bismuth antimony telluride bulk alloys. *Science* **2008,** *320,* 634-638.

32. Zhao, L.-D.; Lo, S.-H.; Zhang, Y.; Sun, H.; Tan, G. J.; Uher, C.; Wolverton, C.; Dravid, V. P.; Kanatzidis, M. G. Ultralow thermal conductivity and high thermoelectric figure of merit in SnSe crystals. *Nature*, **2014,** *508,* 373-377.

33. Zevalkink, A.; Toberer, E. S.; Zeier, W. G.; Flage-Larsen, E.; Snyder, G. J. Ca_3AlSb_3: an inexpensive, non-toxic thermoelectric material for waste heat recovery. *Energy Environ. Sci.* **2011,** *4,* 510-518.